

Functional Segmentation through Dynamic Mode Decomposition: Automatic Quantification of Kidney Function in DCE-MRI Images

Santosh Tirunagari · Norman Poh · Kevin Wells · Mirosław Bober ·
Isky Gordon · David Windridge

Received: date / Accepted: date

Abstract Quantification of kidney function in Dynamic Contrast Enhanced Magnetic Resonance imaging (DCE-MRI) requires careful segmentation of the renal region of interest (ROI). Traditionally, human experts are required to manually delineate the kidney ROI across multiple images in the dynamic sequence. This approach is costly, time-consuming and labour intensive, and therefore acts to limit patient throughput and acts as one of the factors limiting the wider adoption of DCE-MRI in clinical practice.

Therefore, to address this issue, we present the first use of Dynamic Mode Decomposition (DMD) as the basis for automatic segmentation of a dynamic sequence, in this case, kidney ROIs in DCE-MRI. Using DMD coupled combined with thresholding and connected component analysis is first validated on synthetically generated data with known ground-truth, and then applied to ten healthy volunteers DCE-MRI datasets.

Santosh Tirunagari and Norman Poh have benefited from the Medical Research Council (MRC) funded project “Modelling the Progression of Chronic Kidney Disease” under the grant number R/M023281/1.

S. Tirunagari · N. Poh
Department of Computer Science, University of Surrey,
Guildford, Surrey GU2 7XH, UK.
Tel.: +44-(0)1483-6179.

S. Tirunagari · K. Wells · M. Bober
Center for Vision, Speech and Signal Processing (CVSSP),
University of Surrey, Guildford, Surrey GU2 7XH, UK.

I. Gordon
University College London (UCL) Institute of Child Health,
30 Guildford Street, London WC1N 1EH, UK.

D. Windridge
Department of Computer Science, Middlesex University, The
Burroughs, Hendon, London NW4 4BT, UK.

E-mail: {s.tirunagari, n.poh, k.wells, m.bober}@surrey.ac.uk

We find that the segmentation result obtained from our proposed DMD framework is comparable to that of expert observers and very significantly better than that of an a-priori bounding box segmentation. Our result gives a mean Jaccard coefficient of 0.87, compared to mean scores of 0.85, 0.88 and 0.87 produced from three independent manual annotations. This represents the first use of DMD as a robust automatic data driven segmentation approach without requiring any human intervention. This is a viable, efficient alternative approach to current manual methods of isolation of kidney function in DCE-MRI.

Keywords DMD · W-DMD · R-DMD · WR-DMD · DCE-MRI · Movement correction

1 Introduction

Diagnosis of renal dysfunction based on blood and urine tests often produces inaccurate results as the creatinine levels in blood are detectable only after 60% of the renal dysfunction has taken place [34]. Therefore, to address this limitation Dynamic Contrast Enhanced Magnetic Resonance Imaging (DCE-MRI) has been proposed [32, 27]. DCE-MRI is a non-ionising alternative to conventional radioisotope renography. It has particular attraction in cases of Chronic Kidney Disease (CKD), which requires repeated functional assessment, as well as in paediatric cases where exposure to repeated radiation doses is of greater concern than in adults [11, 17, 18]. A further benefit of DCE-MRI is that anatomical images can also be obtained during the same imaging session, providing a direct comparison to the observed physiological abnormalities.

Absolute quantification of kidney (renal) function in DCE-MRI (see Figure 1) is often obscured as it re-

quires manual segmentation [35,36] of the kidney ROI, (i.e., a region of kidney is selected as a template by human experts by manually delineating the kidney ROI). Semi-automatic methods, however, work by specifying the target ROI *a-priori* to an automated segmentation algorithm [9]. Although these approaches are potentially correct, the major issue is the need for human intervention in the segmentation process of the target region. In addition, this can be labour intensive, time-consuming and inefficient as the human expert has to examine the whole sequence of images to find the most suitable frame. This is typically also inconvenient since human experts require proprietary software for delineating the ROI, and also error-prone as the selection of the template (ROI) is subjected to observer variations [19].

Automated methods [10,21] have the potential to overcome these limitations and moreover offer a more reproducible approach. In order to achieve a complete automatic approach reliably, we propose to use Dynamic Mode Decomposition (DMD), which has been used extensively in modelling fluid dynamics. Despite the complexity of the dynamics of an image sequence containing anatomical structures, the information dynamics in our approach are represented in an extremely efficient manner within individual “modes”. These experiments show, for the first time, that DMD can capture distinctive features that clearly distinguish various functional segments within a dynamic MRI image sequence. In this paper, we thus report in detail a framework utilising DMD in conjunction with a simple thresholding technique to obtain functional segmentation of the kidney ROI.

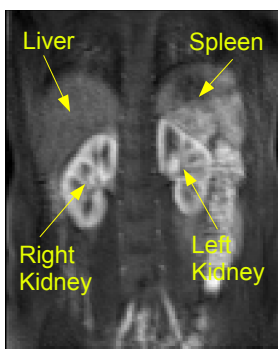


Fig. 1 DCE-MRI image with anatomical parts: *kidney, liver* and *spleen*. Renal perfusion takes place inside the kidney regions after the injection of the contrast agent. The kidney function is then quantified by calculating the mean pixel intensity values inside the kidney region (in practice using a tracer-kinetic method [33]). For this purpose, a proper segmentation of kidney region is required.

Previously, automated segmentation methods utilising clustering and classification methods such as k-means clustering [35] and k-nearest neighbour classification [8] have been suggested. These methods work by considering the signal intensity values across the images in time, thus obtaining a high-dimensional feature vector in each voxel based on the actual tissue response before and after injecting the contrast agent. Methods based on active contours [1] and related methods have also offered solutions that consider the region boundary coupled with shape constraints [2]. A recent work by Hodneland *et al.* in 2014 applied the temporal tissue response and minimal boundary length as shape information for obtaining the kidney segmentation [7] in 4D DCE-MRI videos.

Zollner *et al* [34] introduced the Independent Component Analysis (ICA) technique for functional segmentation of human kidney ROI in DCE-MRI recordings. An approach based on spatio-temporal ICA (STICA) [12] was also developed recently that offers a fully data-driven approach exploiting the distribution of the properties of the spatial data incrementally in the direction of the time axis. A major limitation for this ICA based approach is finding an optimal filter that maximises the statistical independence of the observed signals. The ICA method is typically also approached with a substantial number of assumptions/heuristics and is computationally expensive.

In our previous studies [30], we presented a novel automated, registration-free movement correction approach based on windowed and reconstruction variants of Dynamic Mode Decomposition (WR-DMD) to suppress unwanted complex organ motion in DCE-MRI image sequences caused due to respiration.

Our methodological framework in [30] consisted of the following steps:1) DCE-MRI sequence consisting of N images was processed using the windowed DMD (W-DMD) algorithm in order to output each $N/2$ W-DMD components $C1$ and $C2$. At this stage the W-DMD($C1$) produced the low rank images and W-DMD($C2$) produced sparse images. 2) W-DMD($C1$) was then given as an input to DMD which produced $N/3$ DMD modes. The first 3 DMD modes were then selected for reconstructing the motion stabilised image sequence. Out of the first three dynamic modes, the first mode revealed a low-rank model and the remaining $N - 4$ modes captured the sparse representations. The contrast changes were captured in the most significant modes, in particular, mode-2 was captured kidney region and mode-3 and 4, captured spleen and the liver regions respectively. Noise and residuals including the motion components were captured in the remaining of the modes. Therefore, this study investigates whether we could perform

segmentation of the kidney region of interest from dynamic mode-2 for automatic quantification the kidney function.

Dynamic mode decomposition, due to its ability to identify regions of dominant motion in an image sequence in a completely data-driven manner without relying on any prior assumptions about the patterns of behaviour within the data, has gained significant applications in various fields [28, 29, 5, 3, 16, 4, 31]. Therefore, it is thus potentially be well-suited to analyse a wide variation of blood flow and filtration patterns seen in renography pathology [30].

The novelty of our proposal thus lies in utilising DMD to carry out functional segmentation from medical image sequences in a manner that is both extremely efficient and completely data driven (and thus heuristic-free). Extracting relevant key organs from the DCE-MRI images can potentially provide clinicians with a better way to manage clinical time and cost.

The remainder of this paper is organised as follows: Section 2 considers the theory for DMD as well as presenting evaluation criteria based on Jaccard Similarity Coefficient. Section 3 describes datasets that are based on synthetic data and a set of 10 healthy volunteers' MRI datasets. Section 4 derives our experimental objectives and presents the results and, finally, conclusions are drawn and are discussed in Section 5.

2 Methodology

In this section, we present our methodological framework which consecutively consists of DMD, thresholding, selection of kidney regions using connected component analysis and finally modelling of the kidney function. The overall process pipeline is shown in Figure 2. At the end of this section, we also present our evaluation criteria i.e., Jaccard similarity coefficient for comparing segmentation results.

2.1 Dynamic Mode Decomposition (DMD)

Let $\bar{\mathbf{x}}_r$ be the r^{th} dynamic image frame in a DCE-MRI sequence, whose size is $m \times n$. This image frame $\bar{\mathbf{x}}_r$ is converted to $mn \times 1$ column vector, resulting in the construction of a data matrix \mathbf{X} of size $mn \times N$ for N image frames.

$$\mathbf{X} = [\bar{\mathbf{x}}_1, \bar{\mathbf{x}}_2, \bar{\mathbf{x}}_3, \dots, \bar{\mathbf{x}}_N] = \begin{pmatrix} x_1^1 & x_2^1 & \dots & x_N^1 \\ \vdots & \vdots & \vdots & \vdots \\ x_1^{mn} & x_2^{mn} & \dots & x_N^{mn} \end{pmatrix}. \quad (1)$$

The images in the DCE-MRI data are collected over regularly spaced time intervals and hence each pair of consecutive images are correlated. It can be justified that a mapping A exists between them forming a span of krylov subspace [13, 22, 20]:

$$\begin{aligned} \mathbf{X} &= [\bar{\mathbf{x}}_1, A\bar{\mathbf{x}}_1, A^2\bar{\mathbf{x}}_1, A^3\bar{\mathbf{x}}_1, \dots, A^{N-1}\bar{\mathbf{x}}_1]. \\ [\bar{\mathbf{x}}_2, \bar{\mathbf{x}}_3, \dots, \bar{\mathbf{x}}_N] &= A[\bar{\mathbf{x}}_1, \bar{\mathbf{x}}_2, \dots, \bar{\mathbf{x}}_{N-1}]. \\ \mathbf{P}_2 &= \mathbf{A}\mathbf{P}_1 + \mathbf{r}\mathbf{e}_{N-1}^T. \end{aligned} \quad (2)$$

Here, \mathbf{r} is the vector of residuals that accounts for behaviours that cannot be described completely by \mathbf{A} , $\mathbf{e}_{N-1} = \{0, 0, \dots, 1\} \in \mathcal{R}^{N-1}$, $\mathbf{P}_2 = [\bar{\mathbf{x}}_2, \bar{\mathbf{x}}_3, \dots, \bar{\mathbf{x}}_N]$ and $\mathbf{P}_1 = [\bar{\mathbf{x}}_1, \bar{\mathbf{x}}_2, \dots, \bar{\mathbf{x}}_{N-1}]$. The system \mathbf{A} is unknown and it captures the overall dynamics within the dynamic image sequence in terms of the eigenvalues and eigenvectors of \mathbf{A} , which are referred to as the DMD eigenvalues and DMD modes respectively.

The sizes of the matrices P_2 and P_1 are both $mn \times N - 1$ each. Therefore, the size of unknown matrix A would be $mn \times mn$. Since, matrix A captures the dynamical information within the image sequence, solving it provides us with the dynamics captured in the image sequence in terms of modes. Unfortunately, solving for A is computationally very expensive due to its size. For instance, if an image has a size of 240×320 i.e., $m = 240$ and $n = 320$, the size of A is then 76800×76800 .

From the literature there are two approaches for obtaining these eigenvalues and modes. The first is Arnoldi based approach, which is useful for theoretical analysis due to its connection with Krylov subspace methods [13, 22, 20]. The second is a singular value decomposition (SVD) based approach that is more robust to noise in the data and to numerical errors [24].

Therefore, SVD can be directly applied on \mathbf{P}_1 in Eq. (2), to obtain \mathbf{U} , $\mathbf{\Sigma}$ and \mathbf{V}^* matrices.

$$\mathbf{P}_2 = \mathbf{A}\mathbf{U}\mathbf{\Sigma}\mathbf{V}^*. \quad (3)$$

$$\because \mathbf{P}_1 = \sum_{i=1}^d \Sigma_i \mathbf{u}_i \mathbf{v}_i^*,$$

here, Σ_i is the i^{th} singular value of \mathbf{P}_1 , \mathbf{u}_i and \mathbf{v}_i^* are the corresponding left and right singular vectors respectively; and d is the total number of singular values.

Re-arranging Eq. (3), we obtain the the full-rank matrix \mathbf{A} ,

$$\mathbf{A} = \mathbf{P}_2 \mathbf{V} \mathbf{\Sigma}^{-1} \mathbf{U}^*. \quad (4)$$

Since the eigenvalue analysis is agnostic to any linear projection; so solving the eigen problem of $\tilde{\mathbf{H}}$ is easier than that of solving for \mathbf{A} directly. Moreover, the

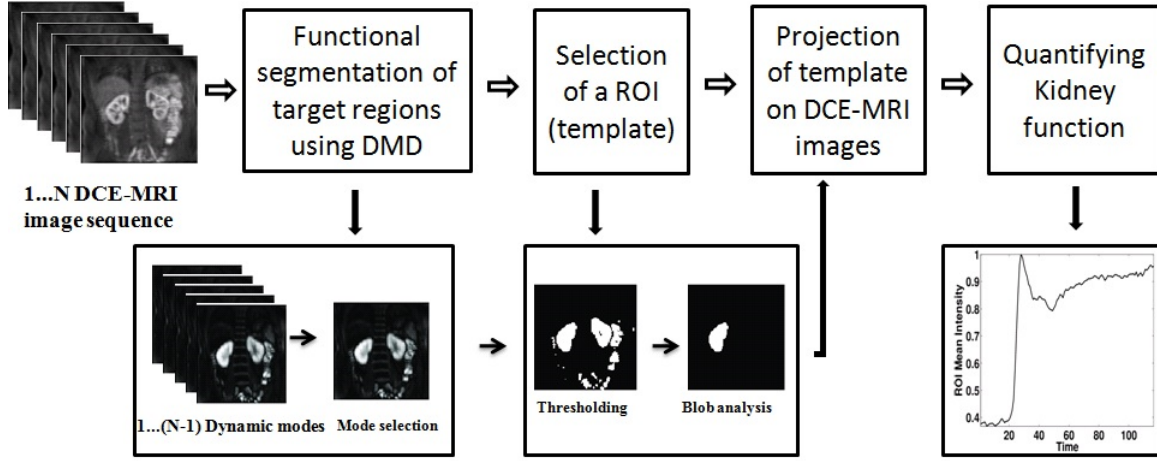


Fig. 2 Flow chart showing the steps involved in the methodological framework. First, a DCE-MRI sequence consisting of N images is processed using the DMD algorithm in order to output $N - 1$ dynamic mode images. From these, we select a dynamic image corresponding to mode 2. Secondly, thresholding is performed for the obtained dynamic mode image and converted to binary image. After binarization, the largest area with connected pixels is selected as a template. Finally, the produced template is projected onto DCE-MRI data to compute the kidney function.

associated eigenvectors of $\tilde{\mathbf{H}}$ provide the coefficients for the linear combination that is necessary to express the dynamics within the time series basis.

$$\tilde{\mathbf{H}}\omega = \sigma\omega, \quad (5)$$

where, ω are the eigenvectors and σ a diagonal matrix containing the corresponding eigenvalues of $\tilde{\mathbf{H}}$ matrix. The eigenvalues of $\tilde{\mathbf{H}}$ approximate some of the eigenvalues of the full system \mathbf{A} [6], we then have:

$$\begin{aligned} \mathbf{A}\mathbf{U} &\approx \mathbf{U}\tilde{\mathbf{H}}, \\ \mathbf{A}\mathbf{U} &\approx \mathbf{U}\omega\sigma\omega^{-1}, \end{aligned} \quad (6)$$

$$\mathbf{A}(\mathbf{U}\omega) \approx (\mathbf{U}\omega)\sigma.$$

Therefore $\tilde{\mathbf{H}}$ is determined on the subspace spanned by the orthogonal singular basis vectors \mathbf{U} obtained via \mathbf{P}_1 ,

$$\tilde{\mathbf{H}} = \mathbf{U}^*(\mathbf{A})\mathbf{U}, \quad (7)$$

$$\tilde{\mathbf{H}} = \mathbf{U}^*(\mathbf{P}_2\mathbf{V}\Sigma^{-1}\mathbf{U}^*)\mathbf{U},$$

which can be rewritten as:

$$\tilde{\mathbf{H}} = \mathbf{U}^*\mathbf{P}_2\mathbf{V}\Sigma^{-1}. \quad (8)$$

Here $\mathbf{U}^* \in \mathbb{C}^{(N-1) \times mn}$ and $\mathbf{V} \in \mathbb{C}^{(N-1) \times (N-1)}$ are the conjugate transpose of \mathbf{U} and \mathbf{V}^* , respectively; and $\Sigma^{-1} \in \mathbb{C}^{(N-1) \times (N-1)}$ denotes the inverse of the singular values Σ . By replacing $\Psi = \mathbf{U}\omega$ in Eq. (6) i.e., $\mathbf{A}(\Psi) \approx (\Psi)\sigma$, we obtain the dynamic modes Ψ . $\therefore \mathbf{U} = \mathbf{P}_2\mathbf{V}\Sigma^{-1}$, therefore, we have:

$$\Psi = \mathbf{P}_2\mathbf{V}\Sigma^{-1}\omega \quad (9)$$

The complex eigenvalues σ contain growth/decay rates and frequencies of the corresponding DMD modes [26, 25]. If σ_j are the diagonal elements of σ from Eq. (5), the temporal behaviour of the DMD modes is then formed via Vandermonde matrix \mathcal{V} , which raises its column vector to the appropriate power. $\mathcal{V}(f)$ with $(N - 1) \times (f + 1)$ elements will be defined by the following:

$$\mathcal{V}(f) = \begin{pmatrix} 1 & \sigma_1^1 & \sigma_1^2 & \dots & \sigma_1^f \\ 1 & \sigma_2^1 & \sigma_2^2 & \dots & \sigma_2^f \\ \vdots & \vdots & \vdots & \vdots & \vdots \\ 1 & \sigma_{N-1}^1 & \sigma_{N-1}^2 & \dots & \sigma_{N-1}^f \end{pmatrix}, \quad (10)$$

$\mathcal{V}(N)$ is a standard Vandermonde matrix for reconstruction but if $f > N$, this is used for forecasting. DMD modes with frequencies μ_j is defined by:

$$\mu_j = \frac{\ln(\sigma_j)}{\delta t}, \quad (11)$$

where δt is the lag between the images. The real part of μ_j regulates the growth or decay of the DMD modes, while the imaginary part of μ_j drives oscillations in the DMD modes.

2.2 Ordering Dynamic modes

In order to select the most significant dynamic modes, the method suggested in [14, 5] is to calculate the logarithmic values of the $diag(\sigma)$. The frequencies which are near origin are the most significant modes. The other way we propose here is by calculating the phase-angles for the complex eigenvalues.

The absolute value for the phase-angles are calculated and modes with unique phase-angles are selected. Doing this will remove one of the conjugate pairs in the dynamic modes. These conjugate modes have same phase-angles but with different signs and look and capture similar information [23]. After discarding one of the conjugate pairs, the dynamic modes are then sorted in ascending order of their phase-angles. The resultant dynamic modes are thus sorted according to their significance. In this study we have considered the first three significant dynamic modes when reconstructing the original sequence.

The effectiveness of DMD, as a preliminary analysis, is demonstrated in Figure 3. The top five figures show random DCE-MRI images in temporal order for a healthy volunteer. Since renal perfusion is taking place inside the kidneys region, one can observe that the corresponding DMD mode in (b) is highlighting the dynamic changes inside the kidney region. A simple thresholding and binarization of the DMD mode thus highlights the kidney region as shown in (c). Selecting the region, or the largest area of connected pixels, can thus give us the kidney template in an exemplar 4D dynamic medical imaging application.

2.3 Performance Measure

To evaluate the performance of our segmentation we use Jaccard similarity coefficient, a standard measure of similarity between finite sample sets [15] (here, in particular, the similarity between the two segmented sets). It is defined as the size of the intersection (of pixels values) between the segmented sets divided by the size of the union of the segmented sets:

$$J(A, B) = \frac{|A \cap B|}{|A \cup B|} \quad (12)$$

Here A and B are two segmented images. Values of the *Jaccard index* range from 0 to 1. (0 if the intersection of the two sets is empty; 1 if the two sets are equal; the more similar the sets are, the closer to 1 is the metric).

2.4 Evaluation Criteria

Let e_i and $d \forall i \in \{1, 2, 3\}$ be the segmented results from the three human experts and DMD framework respectively. For an unbiased evaluation criterion, let us calculate three different ground-truths G_i based on

the segmentation results e_i obtained from the human experts.

$$\begin{aligned} G_1 &= (e_2 \cap e_3), \\ G_2 &= (e_1 \cap e_3) \ \& \\ G_3 &= (e_2 \cap e_1). \end{aligned} \quad (13)$$

The ground-truth for the human expert-1 is the mutual agreement of segmentation results from expert-2 and expert-3. Similarly the ground-truth for expert-2 can be calculated as the mutual agreement of expert-1 and expert-3 and vice versa. The evaluation criteria E_i for the human experts can be calculated as follows:

$$E_i = J(e_i, G_i) = \frac{|e_i \cap G_i|}{|e_i \cup G_i|} \forall i \in \{1, 2, 3\}. \quad (14)$$

The evaluation \mathbf{D} for the DMD framework is given by the average of $D_i \forall i \in \{1, 2, 3\}$:

$$\mathbf{D} = \frac{1}{3} \sum_{i=1}^3 D_i. \quad (15)$$

where,

$$D_i = J(d, G_i) = \frac{|d \cap G_i|}{|d \cup G_i|} \forall i \in \{1, 2, 3\}. \quad (16)$$

3 Dataset

In this section we briefly describe the datasets that we have used in this study i.e., DCE-MRI data and synthetically generated data.

3.1 DCE-MRI data

The functional kidney DCE-MRI datasets used in this study have been provided by collaborators at the Great Ormond Street Hospital using 1.5T Siemens Avanto scanner with 32-channel body phased-array coil. The datasets obtained are from ten healthy volunteers as shown in Figure 4. The acquired DCE-MRI datasets cover the abdominal region, enclosing left and right kidneys and abdominal aorta. The anatomical images can be used to produce organ templates. The dataset consists of 120 MR images taken in sequence for 345 seconds showing the central kidney slice i.e., the largest portion of kidney region.

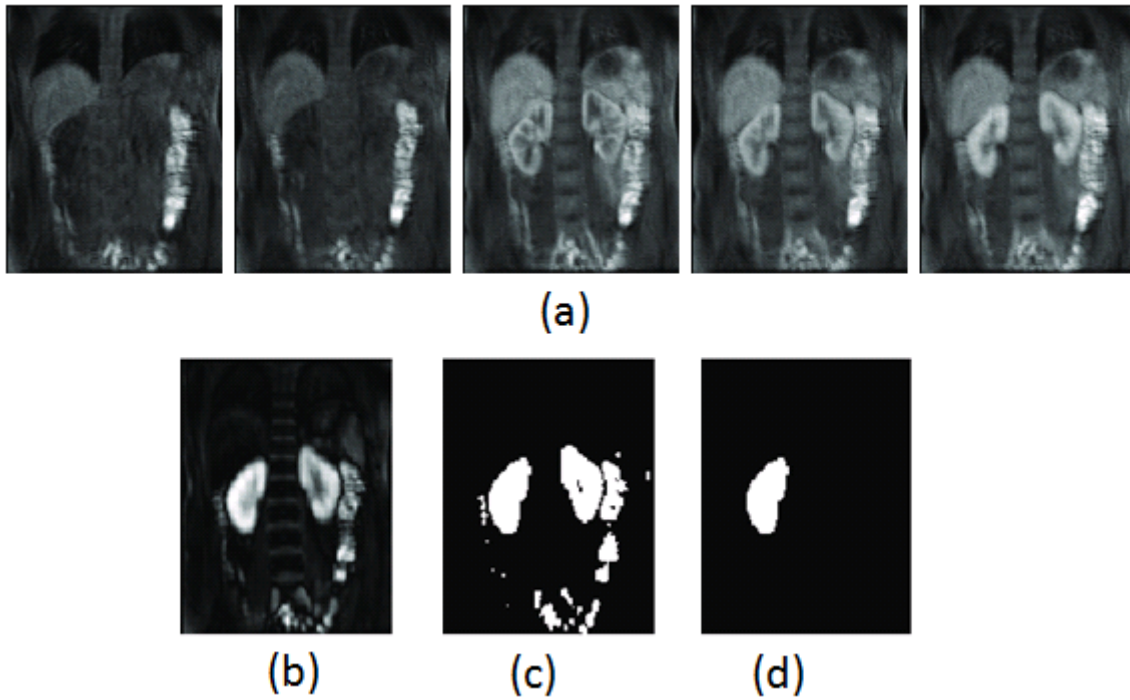


Fig. 3 (a) 5 randomly selected images from a DCE-MRI sequence of a healthy volunteer. The middle image shows the peak stage of renal perfusion inside the kidneys. Quantification of kidney function is performed by calculating the mean of pixel intensity values inside the kidneys. (b) Image showing their corresponding dynamic mode-2. (c) Image showing the binarized version of that dynamic mode. (d) Kidney template with the largest area of connected pixels.

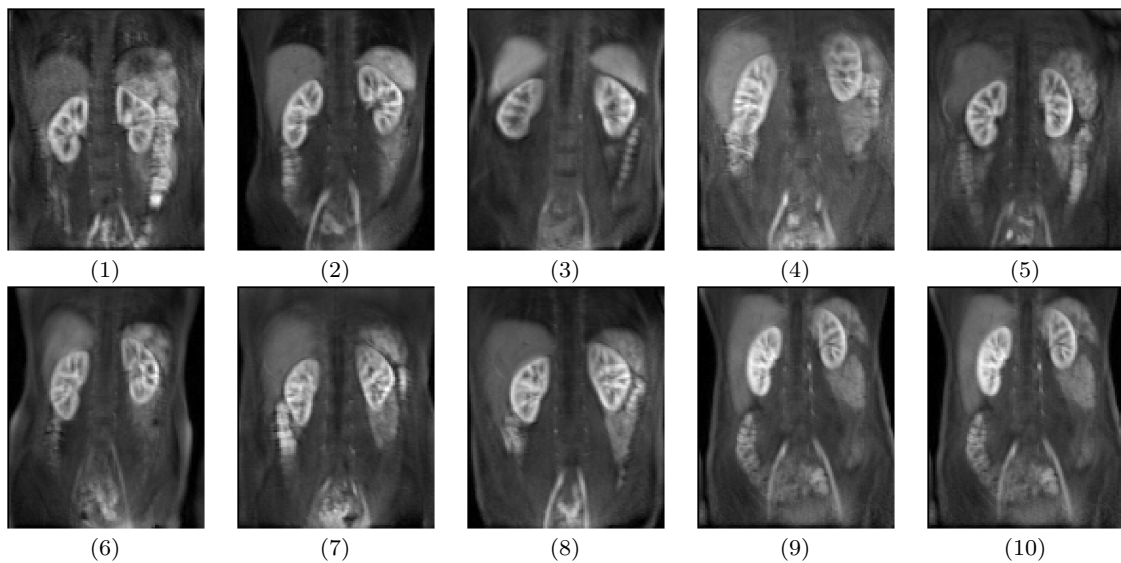


Fig. 4 Exemplars of Dynamic MR images from 10 healthy volunteers' kidney slice produced by DCE-MRI sequence considered as 10 different datasets in this study. The images here show the central kidney slice at time 120s aortic peak enhancement after the contrast agent is injected. The yellow boundary on the kidneys are a results of manual delineation from a human expert. The mean intensity values are calculated in this region across the time producing time-intensity plots.

3.2 Synthetic data

In order to validate our experiments, and to demonstrate the capacity of our framework for functional separation, we artificially generate synthetic data corresponding to broad DCE-MRI events in terms of simple mathematical functions.

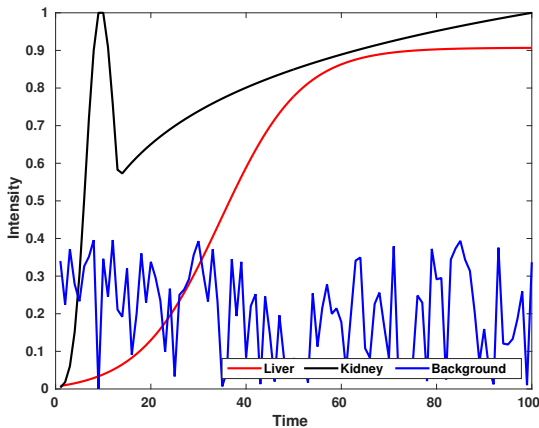


Fig. 5 Graph showing the time and intensity evolution of kidney, liver and background functions.

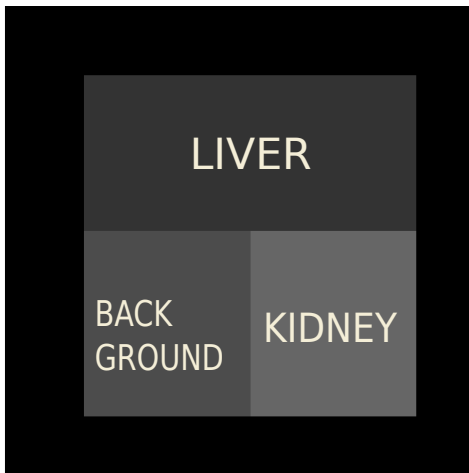


Fig. 6 Simulated image representing kidney, liver and background functions.

A series of 100 images are produced representing the kidney, liver and background functions as labelled in Figure 6 with temporal evolution shown in Figure 5(a). Kidney function is hence modelled as a linear combination of Poisson and log distributions; liver function is modelled as a sigmoid distribution and the background function is derived from a Gaussian noise distribution.

4 Experiments

In this section we outline the experimental procedure as well as the corresponding results.

4.1 Evaluating the DMD framework on synthetically generated data.

We firstly investigate the performance of the proposed framework on the synthetically-generated data embodying a coarse-grained simulation of DCE-MRI composite dynamics. This evaluation will provide the proposed DMD framework with a ground truth and establish the reproducibility and repeatability of our experimental results. Since DMD is completely data-driven, we conjecture that DMD will capture the kidney, liver as well as the background functions within its modes.

Following the outlined methodology, synthetic data consisting of a 100 image sequence is given as an input to the modified DMD algorithm producing 99 DMD modes (In theory, for a image sequence with N images, we obtain $N - 1$ DMD modes). Recall that, in principle, each dynamic mode captures one of the Key dynamic axes of the image sequence. Modes that show pre-dominating liver, kidney and background functions are manually selected, as shown in Figure 7 (top). These modes are then thresholded to obtain the segmented versions of respective functions as shown in Figure 7 (middle). As the DMD is completely data-driven, aside from mode selection (in this case), we have thus demonstrated our conjecture that DMD can capture intact the distinct kidney, liver as well as the background functions from the synthetic data, irrespective of their intrinsically varied morphological kinds. More generally, we have demonstrated the intrinsic capacity of DMD for *functional* separation as distinct from ICA's *stochastic* component separation. We further characterise this separability by projecting the segmented versions of Dynamic modes 1, 2 and 7 for quantifying kidney, liver and background functions as shown in Figure 7(bottom). The Jaccard Similarity Coefficient achieved for synthetic dataset is 1 and Mean Square Error between the DMD result and the ground truth is 0.0000.

4.2 Implementation of the DMD framework on DCE-MRI data

Due to the injection of contrast agent, large scale intensity fluctuations can be observed inside the kidney region which also has minor impact on the liver region. We therefore wish to examine whether these features are indeed picked up by DMD.

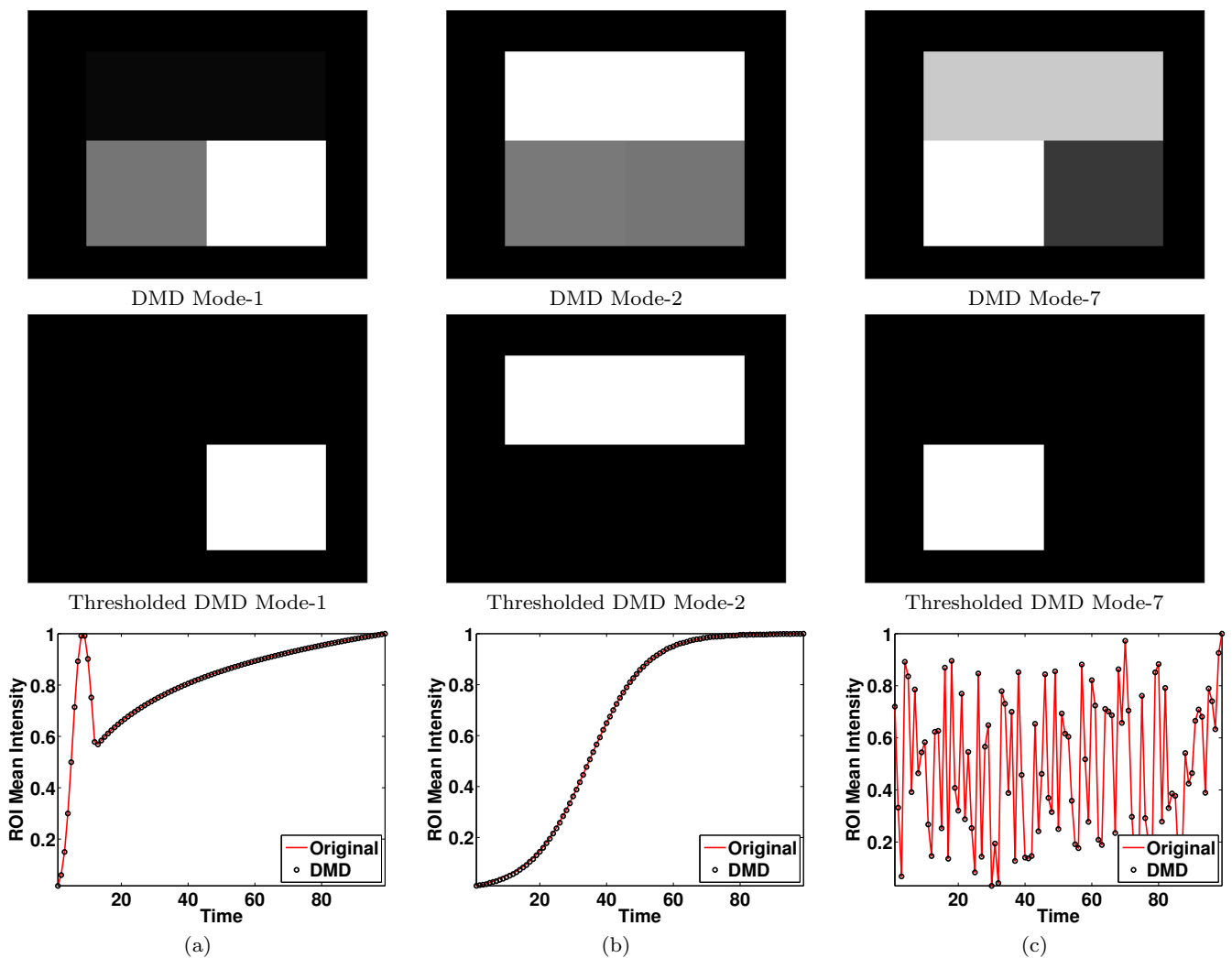


Fig. 7 Selection of DMD modes (top), thresholding (middle), extraction and quantification of (a) kidney, (b) liver and (c) background functions.

DCE-MRI image sequences from the healthy volunteers' data are given as input to DMD algorithm. The output of DMD is thus modally separated large and small scale fluctuations in voxel intensity. These modes are obtained by suppressing the stable information present within the DCE-MRI image sequences (with the exception of mode 1); DMD is thus able to suppress the background information from the image sequence insofar as this is stationary. Renal perfusion (due to the injection of contrast agent) inside the kidney region exhibits large scale voxel intensity fluctuations, followed, in order of magnitude, by liver and spleen region fluctuations respectively. DMD thus captures key kidney, liver and spleen regions in distinct modes as shown in Figure 8. Dynamic mode-1 captures the low-rank image of the DCE-MRI dataset-1 as shown in Figure 8(a) revealing the background function of the dataset. The kidney function is empirically observed to

be captured in dynamic mode-2 (b) and the spleen and liver functions captured in dynamic mode-4 (c) and 5 (d) respectively. The lower order modes reveal the noise components inside the dataset-1 as seen in Figure 8(e). These results hence further provide visual evidence for our conjecture that DMD is capable of isolating key functional regions such as kidney and liver. These rankings however are not given intrinsically by DMD (as discussed previously); we now look at how this can be accomplished.

The main aim in this study is to segment the kidney region so as to enable quantification of the kidney function. We thus select the second dynamic mode for this functional characterisation as this configuration is observed to produce kidney region segmentation, consistent with the above argument, across all of the datasets as shown in Figure 9 (top). These dynamic mode-2s are first normalised in the range of $[0, 1]$. Binarized images

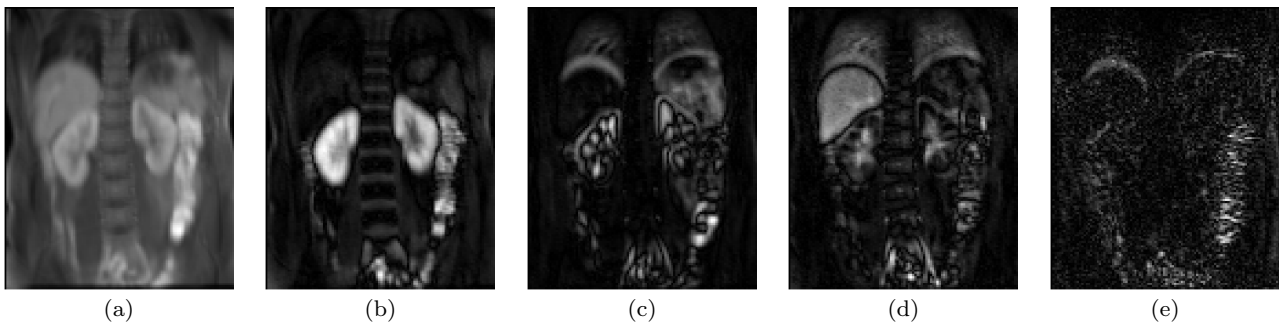


Fig. 8 DMD modes 1,2,4,5 and 83 from a health volunteer’s data (dataset-1). (a) DMD mode-1 showing the background image captured from the dataset. (b) DMD mode-2 showing predominantly the kidney region. (c) DMD mode-4 showing predominantly the spleen region. (d) DMD mode-5 showing predominantly the liver region. (e) DMD mode-83 showing the noise component from the dataset.

of dynamic mode-2s are then obtained by replacing all pixels in the image with intensity values greater than an adaptive threshold with the value 1 (white), and replacing all other pixels with the value 0 (black). These result in the binarized versions of dynamic mode 2 shown in Figure 9 (middle). Kidney templates are then automatically selected as the largest area of connected components of binarized dynamic mode-2 images across all the datasets as shown in Figure 9 (bottom). The connected components are selected by scanning the binarized image from top-to-bottom. All the pixels in a connected component are given a greedy label. Thus, all the pixels in the first connected component are labelled as 1 and those in the second as 2 and so on. These components are then ordered by decreasing area (i.e. the sum of all the pixels present in that particular component) and the label with the largest area is then selected as the kidney template. The produced kidney templates are then projected onto DCE-MRI images to obtain the kidney function (as shown in Figure 2 from Section 2) by calculating the mean intensity pixel values inside region specified by the template. The kidney functions across all the datasets obtained through the DMD framework are shown in Figure 10.

4.3 Evaluation of the DMD framework on DCE-MRI.

Evaluation of our framework is two-fold:

- Evaluation of the performance of the segmented kidney template.
- Evaluation of the performance of the quantified kidney function.

After obtaining the kidney ROIs (i.e the templates), the Jaccard Similarity Measure is used to evaluate the performance of the proposed DMD framework with respect to the ground-truth data. The aim of this exper-

iment is to benchmark the generalisation performance of our framework against expert annotations.

For an unbiased evaluation, three different ground-truths $G_i \forall i \in \{1, 2, 3\}$ are calculated based on the three different segmentation results obtained from the human experts. The ground-truth G_1 for the human expert-1 is calculated as the mutual agreement of the segmentation between expert-2 and expert-3. Similarly the ground-truth G_2 for expert-2 is calculated as the mutual agreement of segmentation between expert-1 and expert-3 and vice versa. We also have considered an additional baseline given by the minimum bounding box region around the human annotated regions (to simulate ‘blind’ *a priori* segmentation). The DMD framework is evaluated as the mean of JSC values from all three ground-truths. Table 1 shows the JSC values for the DMD framework against the three ground-truths $G_i \forall i \in \{1, 2, 3\}$. The last column of the table presents the mean of the JSC values obtained from the three ground-truths across all the 10 datasets.

Table 1 Evaluation results for the DMD framework with respect to the three ground-truths $G_i \forall i \in \{1, 2, 3\}$.

	G_1	G_2	G_3	avg(DMD)
Dataset-1	0.8789	0.8672	0.8727	0.8729
Dataset-2	0.8291	0.8525	0.8758	0.8525
Dataset-3	0.8426	0.8628	0.8411	0.8488
Dataset-4	0.9038	0.9133	0.9279	0.9150
Dataset-5	0.8583	0.9027	0.8854	0.8821
Dataset-6	0.8651	0.8418	0.8386	0.8485
Dataset-7	0.8578	0.8239	0.8065	0.8294
Dataset-8	0.8927	0.9075	0.8861	0.8954
Dataset-9	0.8949	0.8702	0.8828	0.8826
Dataset-10	0.8356	0.8169	0.8799	0.8441

The performance of the kidney segmentation achieved by the DMD framework, the blind bounding-box region and three domain experts with respect to their ground-truths are reported in Table 2. The JSC values

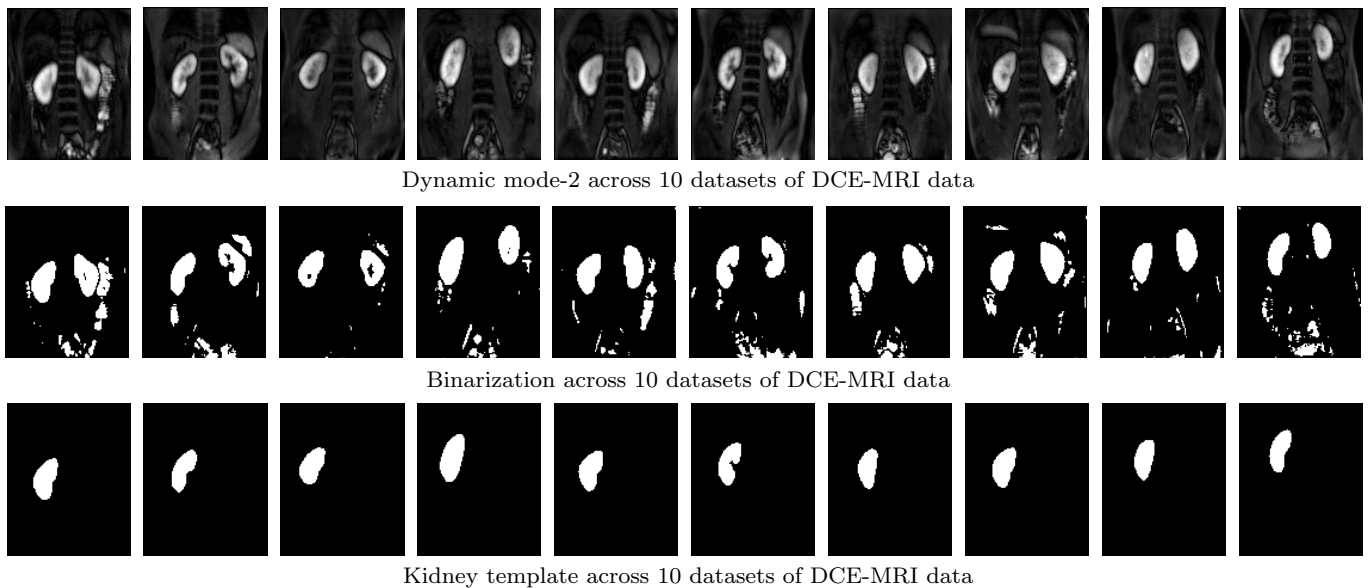


Fig. 9 (Top) Image showing the kidney regions in Dynamic mode-2 across the 10 datasets used in this study. (Middle) Images showing the binarization effect on dynamic mode-2 across the datasets. (Bottom) Images showing the kidney template selected by the largest area of connected components.

achieved by expert-2 are generally high in comparison to the other experts. The DMD framework has achieved higher JSC values 0.91, 0.89 & 0.88 for the datasets 4 and 8 and 9. The Overall average JSC values for the experts are 0.85, 0.87 & 0.87 and for the DMD framework is around 0.86 while for minimum bounding-box region the JSC is below 0.04

Table 2 Jaccard similarity coefficients for kidney segmentation achieved by the DMD framework, blind bounding-box region and three domain experts with respect to the ground-truth

	DMD	E-1	E-2	E-3	Bbox
D-1	0.8729	0.8642	0.8994	0.8974	0.5891
D-2	0.8525	0.8718	0.8925	0.8906	0.4563
D-3	0.8488	0.8642	0.8781	0.8719	0.4298
D-4	0.9150	0.8880	0.8894	0.8894	0.4073
D-5	0.8821	0.8668	0.9064	0.8934	0.3162
D-6	0.8485	0.8589	0.8679	0.8536	0.3016
D-7	0.8294	0.8548	0.8833	0.8529	0.2692
D-8	0.8954	0.8155	0.8726	0.8708	0.2984
D-9	0.8826	0.8221	0.8711	0.8391	0.2624
D-10	0.8441	0.8426	0.8292	0.8792	0.2455
avg	0.8671	0.8548	0.8789	0.8738	0.3575

Figure 10 shows the kidney functions produced by the DMD framework, ground-truth ($G_i \forall i \in \{1, 2, 3\}$), three domain experts as well as kidney function produced by blind bounding-box over the kidney region. The results in these figures show that kidney function quantified by DMD is closely aligned with the experts annotation.

Evaluation for the kidney functions are calculated based on the Mean Square Error (MSE) criteria as shown in Table 3.

Table 3 Mean Square Error (MSE) based evaluation of the kidney functions for DMD, human experts and the bounding box.

	avg (DMD)	E-1	E-2	E-3	avg (Bbox)
D-1	0.0001	0.0001	0.0001	0.0000	0.0029
D-2	0.0001	0.0001	0.0001	0.0000	0.0126
D-3	0.0002	0.0001	0.0001	0.0000	0.0082
D-4	0.0000	0.0000	0.0001	0.0001	0.0085
D-5	0.0001	0.0000	0.0000	0.0000	0.0166
D-6	0.0000	0.0000	0.0000	0.0000	0.0188
D-7	0.0001	0.0001	0.0001	0.0000	0.0162
D-8	0.0001	0.0002	0.0000	0.0000	0.0431
D-9	0.0000	0.0002	0.0001	0.0000	0.0176
D-10	0.0000	0.0000	0.0002	0.0001	0.0213

drvdk144@gmail.com

5 Discussions & Conclusions

This study aims to demonstrate the significance of the proposed DMD framework as a viable functional segmentation algorithm when coupled with simple thresholding-binarization and selection of the largest area of connected pixels to effectively quantify kidney function in DCE-MRI data. We applied the DMD framework to 10 sets of DCE-MRI data collected from healthy volun-

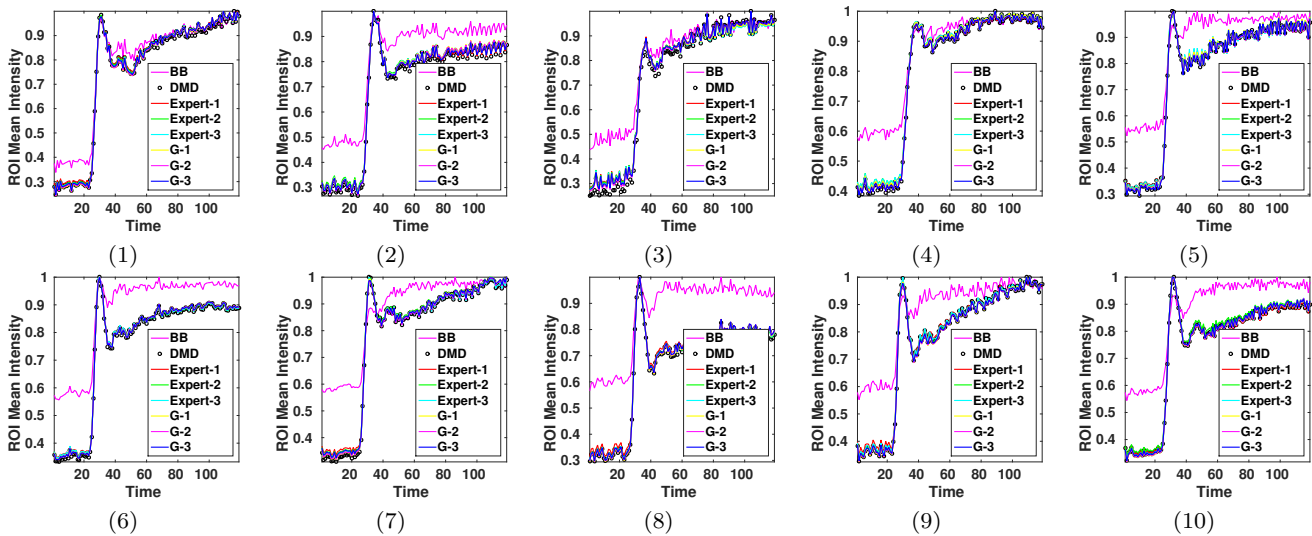


Fig. 10 Kidney function produced by blind bounding-box region, DMD framework, three domain experts and ground-truths for datasets 1-10.

teers. We also applied the DMD framework to synthetically generated data mimicking the DCE-MRI data. The results demonstrate that the proposed framework is extremely promising in obtaining functional segmentation in general and thus to quantifying segmented functions, in particular kidney functionality.

DMD can be demonstrated to extract local variations as a low rank representation within an image sequence, as well as capturing dominating regions of causally-connected intensity fluctuations. In our context, perfusion inside the kidney region is the most dominating region of intensity fluctuations due to the injection of contrast agent. DMD was thus able to naturally capture the kidney region as mode-2. Using a simple thresholding technique and selecting the largest area with connected pixels then automatically generates the proposed kidney region. The results for the proposed DMD framework when compared with expert annotations and ground-truth clearly shows the strength of the framework suggesting that manual selection of kidney region is no longer needed and that the entire process can be automated.

Acknowledgements The funding for this work has been provided by the Department of Computer Science and the Centre for Vision, Speech and Signal Processing (CVSSP) - University of Surrey. ‘I.G.’ would like to express gratitude towards Kidney Research UK for funding the DCE-MRI data acquisition as part of a reproducibility study. ‘S.T.’ and ‘N.P.’ have benefited from the Medical Research Council (MRC) funded project “Modelling the Progression of Chronic Kidney Disease” under the grant number R/M023281/1. The details of the project are available at www.model11ingCKD.org. ‘D.W.’ acknowledges the financial support from the Horizon 2020 European Research project “DREAMS4CARS” (#731593).

References

- Abdelmunim, H., Farag, A., Miller, W., AboelGhar, M., et al.: A kidney segmentation approach from dce-mri using level sets. In: Computer Vision and Pattern Recognition Workshops, 2008. CVPRW’08. IEEE Computer Society Conference on, pp. 1–6. IEEE (2008)
- Ali, A.M., Farag, A.A., El-Baz, A.S.: Graph cuts framework for kidney segmentation with prior shape constraints. In: Medical Image Computing and Computer-Assisted Intervention–MICCAI 2007, pp. 384–392. Springer (2007)
- Berger, E., Sastuba, M., Vogt, D., Jung, B., Amor, H.B.: Dynamic mode decomposition for perturbation estimation in human robot interaction. In: The 23rd IEEE International Symposium on Robot and Human Interactive Communication, pp. 593–600 (2014). DOI 10.1109/ROMAN.2014.6926317
- Brunton, B.W., Johnson, L.A., Ojemann, J.G., Kutz, J.N.: Extracting spatial-temporal coherent patterns in large-scale neural recordings using dynamic mode decomposition. *Journal of neuroscience methods* **258**, 1–15 (2016)
- Grosek, J., Kutz, J.N.: Dynamic mode decomposition for real-time background/foreground separation in video. arXiv preprint arXiv:1404.7592 (2014)
- Grosek, J., Kutz, J.N.: Dynamic mode decomposition for real-time background/foreground separation in video. *CoRR abs/1404.7592* (2014). URL <http://arxiv.org/abs/1404.7592>
- Hodneland, E., Hanson, E., Lundervold, A., Modersitzki, J., Eikefjord, E., Munthe-Kaas, A.Z., et al.: Segmentation-driven image registration-application to 4d dce-mri recordings of the moving kidneys. *Image Processing, IEEE Transactions on* **23**(5), 2392–2404 (2014)
- Hodneland, E., Kjørstad, Å., Andersen, E., Monssen, J.A., Lundervold, A., Rorvik, J., Munthe-Kaas, A.: In vivo estimation of glomerular filtration in the kidney using dce-mri. In: Image and Signal Processing and Analysis (ISPA), 2011 7th International Symposium on, pp. 755–761. IEEE (2011)

9. Huang, A.J., Lee, V.S., Rusinek, H.: Functional renal mr imaging. *Magnetic resonance imaging clinics of North America* **12**(3), 469–486 (2004)
10. Johnson, S., Rishi, R., Andone, A., Khawandi, W., Al-Said, J., Gletsu-Miller, N., Lin, E., Baumgarten, D.A., O'Neill, W.C.: Determinants and functional significance of renal parenchymal volume in adults. *Clinical Journal of the American Society of Nephrology* **6**(1), 70–76 (2011)
11. Khrichenko, D., Darge, K.: Functional analysis in mr urographymade simple. *Pediatric radiology* **40**(2), 182–199 (2010)
12. Kiani, S., Gordon, I., Windridge, D., Wells, K.: On-line spatio-temporal independent component analysis for motion correction in renal dce-mri. In: *Nuclear Science Symposium and Medical Imaging Conference (NSS/MIC)*, 2012 IEEE, pp. 2910–2915. IEEE (2012)
13. Krylov, A.: On the numerical solution of the equation by which in technical questions frequencies of small oscillations of material systems are determined. *Izvestija AN SSSR (News of Academy of Sciences of the USSR), Otdel. mat. i estest. nauk* **7**(4), 491–539 (1931)
14. Kutz, J.N., Fu, X., Brunton, S.L.: Multiresolution dynamic mode decomposition. *SIAM Journal on Applied Dynamical Systems* **15**(2), 713–735 (2016)
15. Levandowsky, M., Winter, D.: Distance between sets. *Nature* **234**(5323), 34–35 (1971)
16. Mann, J., Kutz, J.N.: *Dynamic Mode Decomposition for Financial Trading Strategies*. ArXiv e-prints (2015)
17. Michaely, H., Herrmann, K., Nael, K., Oesingmann, N., Reiser, M., Schoenberg, S.: Functional renal imaging: nonvascular renal disease. *Abdominal imaging* **32**(1), 1–16 (2007)
18. Prasad, P.V.: Functional mri of the kidney: tools for translational studies of pathophysiology of renal disease. *American Journal of Physiology-Renal Physiology* **290**(5), F958–F974 (2006)
19. de Priester, J.A., den Boer, J.A., Giele, E.L., Christiaans, M.H., Kessels, A., Hasman, A., van Engelshoven, J.: Mr renography: an algorithm for calculation and correction of cortical volume averaging in medullary renographs. *Journal of Magnetic Resonance Imaging* **12**(3), 453–459 (2000)
20. Ruhe, A.: Rational krylov sequence methods for eigenvalue computation. *Linear Algebra and its Applications* **58**, 391–405 (1984)
21. Rusinek, H., Boykov, Y., Kaur, M., Wong, S., Bokacheva, L., Sajous, J.B., Huang, A.J., Heller, S., Lee, V.S.: Performance of an automated segmentation algorithm for 3d mr renography. *Magnetic Resonance in Medicine* **57**(6), 1159–1167 (2007)
22. Saad, Y.: Krylov subspace methods for solving large unsymmetric linear systems. *Mathematics of computation* **37**(155), 105–126 (1981)
23. Sayadi, T., Schmid, P., Nichols, J., Moin, P.: Dynamic mode decomposition of controlled h-and k-type transitions. *Annual Research Briefs (Center for Turbulence Research, 2013)* p. 189 (2013)
24. Schmid, P., Li, L., Juniper, M., Pust, O.: Applications of the dynamic mode decomposition. *Theoretical and Computational Fluid Dynamics* **25**(1-4), 249–259 (2011)
25. Schmid, P.J.: Dynamic mode decomposition of numerical and experimental data. *Journal of Fluid Mechanics* **656**, 5–28 (2010)
26. Schmid, P.J., Meyer, K.E., Pust, O.: Dynamic mode decomposition and proper orthogonal decomposition of flow in a lid-driven cylindrical cavity. In: *8th International Symposium on Particle Image Velocimetry*, pp. 25–28 (2009)
27. Sourbron, S.P., Buckley, D.L.: Classic models for dynamic contrast-enhanced mri. *NMR in Biomedicine* **26**(8), 1004–1027 (2013)
28. Tirunagari, S., Poh, N., Bober, M., Windridge, D.: Windowed dmd as a microtexture descriptor for finger vein counter-spoofing in biometrics. In: *Information Forensics and Security (WIFS)*, 2015 IEEE International Workshop on. IEEE (2015)
29. Tirunagari, S., Poh, N., Bober, M., Windridge, D.: Can dmd obtain a scene background in color? In: *Image, Vision and Computing (ICIVC)*, International Conference on, pp. 46–50. IEEE (2016)
30. Tirunagari, S., Poh, N., Wells, K., Bober, M., Gorden, I., Windridge, D.: Movement correction in dce-mri through windowed and reconstruction dynamic mode decomposition. *Machine Vision and Applications* **28**(3), 393–407 (2017). DOI 10.1007/s00138-017-0835-5. URL <http://dx.doi.org/10.1007/s00138-017-0835-5>
31. Tirunagari, S., Poh, N., Windridge, D., Iorliam, A., Suki, N., Ho, A.T.: Detection of face spoofing using visual dynamics. *Information Forensics and Security, IEEE Transactions on* **10**(4), 762–777 (2015)
32. Tofts, P.S.: T1-weighted dce imaging concepts: modelling, acquisition and analysis. *signal* **500**(450), 400 (2010)
33. Tofts, P.S., Cutajar, M., Mendichovszky, I.A., Peters, A.M., Gordon, I.: Precise measurement of renal filtration and vascular parameters using a two-compartment model for dynamic contrast-enhanced mri of the kidney gives realistic normal values. *European radiology* **22**(6), 1320–1330 (2012)
34. Zöllner, F.G., Kocinski, M., Lundervold, A., Rørvik, J.: Assessment of renal function from 3d dynamic contrast enhanced mr images using independent component analysis. In: *Bildverarbeitung für die Medizin 2007*, pp. 237–241. Springer (2007)
35. Zöllner, F.G., Sance, R., Rogelj, P., Ledesma-Carbayo, M.J., Rørvik, J., Santos, A., Lundervold, A.: Assessment of 3d dce-mri of the kidneys using non-rigid image registration and segmentation of voxel time courses. *Computerized Medical Imaging and Graphics* **33**(3), 171–181 (2009)
36. Zöllner, F.G., Svarstad, E., Munthe-Kaas, A.Z., Schad, L.R., Lundervold, A., Rørvik, J.: Assessment of kidney volumes from mri: acquisition and segmentation techniques. *American Journal of Roentgenology* **199**(5), 1060–1069 (2012)